A Localization Method for Untethered Small-Scale Robots using Electrical Impedance Tomography

Hugo Daguerre, Sinan Demir, Utku Culha, François Marionnet, Michaël Gauthier, Metin Sitti, Aude Bolopion

A Localization Method for Untethered Small-Scale Robots using Electrical Impedance Tomography

Hugo Daguerre[1‡], Sinan O. Demir[2,3‡], Utku Culha[2,4], Francois Marionnet[1], Michaël Gauthier[1], Metin Sitti[2,5], *Fellow IEEE*, and Aude Bolopion[1]

***Abstract*—Untethered small-scale robots can be potentially used in medical applications such as minimally invasive surgeries and targeted drug delivery. This paper introduces a new localization method using Electrical Impedance Tomography (EIT), which is an emerging medical imaging technique, to dynamically track small-scale robots. The proposed approach provides the electrical conductivity distribution within the robot workspace from a set of electrical stimulations and voltage measurements gathered from eight electrodes placed at its boundary. The position of the robot can be deduced from the conductivity map that is reconstructed with the contrast in electrical properties between the robot and the background medium. This method is experimentally validated by successfully tracking the 2D motion of 4 different magnetically actuated robots within a cylindrical arena (30 mm in diameter and 4.2 mm high). The smallest detected robot is 1.5 $\times$ 1.5 $\times$ 1 mm^3. The proposed tracking method provides a non-invasive technology with low-cost and high-speed potential that would be significant and useful for the position feedback control of untethered devices for biomedical applications in the future.**

***Index Terms*—Microrobotics, position tracking, electrical impedance tomography, magnetic actuation.**

I. Introduction

SMALL robots (i.e., robots $< 1\,\mathrm{cm}$) capable of navigating in a controlled manner through confined and enclosed spaces have been extensively studied in recent years to enable applications in various domains such as micromanipulation [1], [2] and healthcare [3], [4]. Among magnetic [2], optical [5], acoustic [6] and biological [7] actuation approaches used for mobile small-scale robots, the magnetic actuation method becomes more prominent for medical applications due to its potential usage inside nontransparent environments, and deep penetration capability in any nonmagnetic media [8]. After a rapid development in the past decade and the demonstration of applications in optically transparent environments, the scientific interest in deploying such small-scale robots into other workspaces is strong and growing [9]. However, ensuring the efficiency of delicate tasks at small scale requires a precise control over robot motion and positioning. Achieving such a fine and consistent control in spite of perturbations and model uncertainties implies the need of a position feedback. Therefore, the potential of untethered small robots to become a real breakthrough in applied medicine strongly depends on the ability to provide suitable localization techniques.

To address this challenge, several methods have been studied in the last few years. These methods are extensively reviewed by recent articles reflecting the interest of the community in the subject [10]–[12]. Various technologies that are well-established in biomedical imaging have been explored for the tracking of small-scale robots such as magnetic field-based techniques [13]–[15], ultrasound [16], [17], optical techniques [18], [19] and ionizing radiation-based methods [20], [21]. Although these solutions are promising, a large part of the existing technologies still exhibit some limitations in terms of cost, scanning speed, penetration depth, and adverse health effects [10]–[12].

Alternatively to these conventional methods, the exploitation of electrical impedance variations has recently shown to be relevant for localization purposes at small scale [22], [23]. At the macroscopic level, simulation results from Snyder et al. [24] suggest that Electrical Impedance Tomography (EIT) would be of interest to track underwater objects. EIT exploits electrical stimulations and measurements made through the surface of an object to non-invasively image the interior of a domain by estimating the internal distribution of the electrical properties. The underlying principles of this technique were first applied in geophysical exploration to detect conductive ore or liquids in the ground [25]. Thereafter, EIT has been used in medicine to image various physiological phenomena such as breathing [26], cardiac function [27], or brain activity [28]. These applications show that EIT is a safe imaging technique, unlike the prolonged use of ionizing radiations (eg., X-rays). It also illustrates the possibility to image deep tissues, contrary to optical techniques that are limited to superficial areas [10]. Moreover, EIT systems can provide high-speed imaging [29] with low-cost [30], and high portability [31] (ie., no cumbersome equipment). These aspects make EIT an attractive technique toward microrobot localization in the context of biomedical applications.

While the exploitation of electrical impedance changes in robotics had been so far limited to tactile human-robot

‡ These authors contributed equally to this work.

[1] Authors are with FEMTO-ST Institute, CNRS, Univ. Bourgogne Franche-Comté, 24 rue Alain Savary, F-25000 Besançon, France. E-mail: aude.bolopion@femto-st.fr.

[2] Authors are with the Physical Intelligence Department, Max Planck Institute for Intelligent Systems, 70569 Stuttgart, Germany.

[3] Author is with the Stuttgart Center for Simulation Science (SC SimTech), University of Stuttgart, 70569 Stuttgart, Germany.

[4] Current affiliation: Munich School of Robotics and Machine Intelligence, Technical University of Munich, 80797 Munich, Germany.

[5] Author is with the Institute for Biomedical Engineering, ETH Zurich, 8092 Zurich, Switzerland

Manuscript received Aug 10, 2021; revised Nov 15, 2021.

interactions [32], [33] and on-board deformability sensing [34], [35], this article describes a new robot tracking system based on EIT. The possibility to localize untethered small-scale robots in 2D using EIT is demonstrated through in vitro experiments, where the actuation of the robot is achieved by an external magnetic field and a camera is used to verify the tracking performance. It is shown by static experiments that the EIT tracking system and the applied magnetic field do not interfere. Moreover, to evaluate the influence of the size of the robot on the tracking accuracy, multiple robots in changing sizes are fabricated and tested. The primary contributions of this work are:

- The first use of EIT to track the dynamic motions of small-scale robots.
- A tracking system decoupled from magnetic actuation.
- A method suitable for localization in non-homogeneous environments.
- The study of the tracking accuracy and the determination of the smallest detectable robot.

This paper is organized as follows. Section II introduces the working principle of the EIT technique. In Section III, the experimental platform including the robot design, actuation and optical tracking system is presented. Section IV provides a detailed description of the proposed EIT localization system. Section V introduces the results of the robot tracking experiments and analyzes the accuracy of the developed system according to the size of the robot, EIT reconstruction parameters, and different environments. Section VI discusses the capacity of the proposed system and presents challenges and future possibilities in the use of EIT technology for monitoring and tracking micromachines.

II. Electrical Impedance Tomography

Tomography is a technique used to estimate the internal structure of an object from signals emitted and measured outside the analyzed domain [36]. Among various tomographic methods based on different physics, EIT relies on electricity to non-invasively reconstruct the interior of the target. The electrical measurements and excitations (i.e., voltages or currents) are typically performed by means of multiple electrodes placed on the surface of the system to be imaged. This set of signals is then used to determine the distribution of the absolute conductivity (absolute EIT) within a 2D or 3D domain, or the distribution of the conductivity changes with respect to a reference state (difference EIT) [36]. This section presents the theoretical fundamentals of EIT. It enters the category of inverse problems, which require finding the model parameters (causes) that correspond to the observations (effects) as well as possible (Fig. 1).

A. EIT Forward Problem

The forward problem reflects the influence of the model parameters on the measurements. It determines the electrical voltages V_i measured at different positions i on the boundary of the system from the knowledge of the internal conductivity distribution σ and the stimulating current injection.

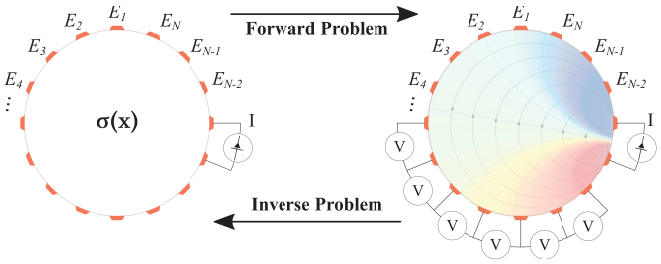

Fig. 1. Principle of EIT. An electrical stimulation is applied through the boundary of the studied domain and the resulting voltages are measured. The forward problem provides the measurements from the knowledge of the medium properties, while the inverse problem estimates the medium properties from the measurements.

From Maxwell's equations, it is possible to show that the electrical potential u inside the domain studied Ω is governed by [37]:

$$\nabla \cdot \gamma(x,\omega)\nabla u(x) = 0, \tag{1}$$

where x is a point in Ω, ω is the angular frequency of the applied current, and γ is the electric admittivity given by $\gamma(x,\omega) = \sigma(x,\omega) + i\omega\varepsilon(x,\omega)$, where σ is the electric conductivity and ε is the permittivity. In the conventional frequency range at which EIT systems operate, the imaginary part of the admittivity is usually negligible [36]. Therefore, γ is approximated to the conductivity σ.

In addition to (1), the formulation of the forward problem includes conditions on the current density j which is related to the potential by Ohm's law $j = \sigma\nabla u$, and satisfies:

$$\int_{\partial\Omega} j dS = 0, \tag{2}$$

which implies that electrical charges do not accumulate locally within the medium. In other words, all the currents injected into Ω necessarily flow out.

Additional boundary conditions are set to account for the known electrical stimulation at given electrodes. Their formulation depends on the modeling of the electrode-medium interface. This interface can be modeled in a multitude of ways with varying degrees of precision and complexity [38].

The forward problem can be solved using standard numerical methods including the Finite Element Method (FEM) [39]. The goal in EIT is to find a conductivity distribution in Ω such that the resulting forward solution is as close as possible to the signals measured experimentally. This corresponds to solving the inverse problem.

B. Inverse Problem and Image Reconstruction

Solving the inverse problem requires finding a value of the conductivity σ that minimizes the data mismatch between the electrical measurements y and their estimates via the forward solution $F(\sigma)$ [36]

$$\|y - F(\sigma)\|^2. \tag{3}$$

However, unlike the forward problem, EIT inverse problem is ill-posed, which means that it is particularly complex to

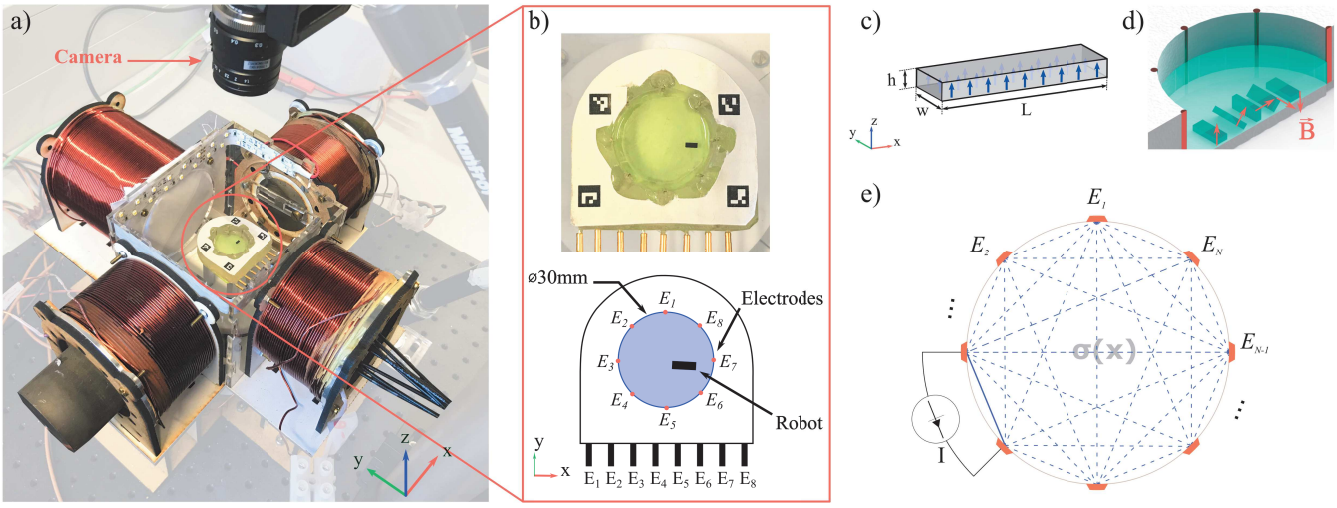

Fig. 2. (a) Photo of the magnetic actuation system with 5 electromagnetic coils (4 of them placed on XY-plane, while the 5^{th} is below the test area), the test area surrounded by the 8 electrodes of the EIT system and a high-speed camera that allows generating the ground truth data. (b) Top view photo and drawing of the test area showing the electrode positions and a sample robot in the test fluid. (c) Uniform magnetization profile of the magnetic small-scale robot along its body (blue arrows). (d) Sample movement of the magnetic small-scale robot by applying a rotating magnetic field B shown by red arrows. (e) Illustration of the full scan EIT stimulation scheme. All electrode pairs are successively selected as driving electrodes.

solve because of the non-uniqueness and the instability of the solution [38].

Although the determination of an inverse solution remains an open subject, various resolution approaches have been proposed [40]. The most popular is based on the linearization and the regularization of the problem to get an approximated well-posed problem. The equation to minimize becomes [36]

$$\|y - F(\sigma)\|_W^2 + \lambda^2 \|\sigma - \sigma_0\|_Q^2 , \tag{4}$$

where W is a data weighting matrix representing the inverse covariance of measurements, σ_0 is an *a priori* estimate of the solution, Q is the regularization matrix that can contain certain prior assumptions about the solution and the 2-norm represented as $\|a\|_A^2 = a^T A a$. The regularization process introduces extra information to promote some credible solutions. It involves a trade-off between the prior solution and the exact solution based on the measured data. The balance of this trade-off is controlled by the hyperparameter λ.

Interestingly, the regularization process can also be defined such that both spatial and temporal information are added. This is possible in the case of non-stationary applications, when successive frames are not independent provided the acquisition rate is sufficient with respect to the dynamic of the observed phenomenon. Such a spatio-temporal resolution approach has been developed in [41].

This is particularly relevant for robot tracking purposes (see Section V). Herein, the solver developed in [41] is utilized for the proof-of-concept of an EIT-based position sensor for untethered small-scale robots.

III. Experimental Robot System

The applicability of the proposed EIT-based tracking method on the untethered small-scale robots is tested by using the experimental setup and the small-scale robot design shown in Fig. 2.

A. Robot Design, Fabrication and Gait Definition

The magnetic small-scale robots used in this study are fabricated following the methods reported in [42] and [43]. To start with, Ecoflex 00-30 (Smooth-On Inc.) and neodymium-iron-boron (NdFeB) magnetic particles with 5 µm diameter (MQFP-15-7, Magnequench) are mixed with a 1:1 body mass ratio. Then, the pre-polymer mixture is poured on a methyl methacrylate plate and two sets of six robots (dimensions are provided in Table I) are cut out of the cured polymer sheet using a high-resolution laser cutter (LPKF Protolaser U4). The first set of robots are kept non-magnetized and used to avoid any influence of the motion of the robot in the experiments studying the impact of the magnetic field on the EIT data (Section V-A). The second set of robots, on the other hand, are put into flat molds and magnetized within a magnetic field with a magnitude of 1.8 T pointing parallel to the vertical axis of the robots. Once the robots are taken out of the molds, the magnetic particles maintain their magnetization orientation forming a uniform profile along the longitudinal axis of the robot body as shown in Fig. 2c.

To test the accuracy of the proposed tracking method for dynamic cases in Section V-B, fabricated robots are magnetically actuated to move in the workspace by rolling locomotion. Each cycle of the applied rotating magnetic field B around

TABLE I
Dimensions of the Small-Scale Robots

	L (mm)	w (mm)	h (mm)	V (mm^3)
R1	5.23	2.12	1.00	11.09
R2	3.70	1.50	1.00	5.55
R3	2.77	1.12	1.00	3.10
R4	1.50	1.50	1.00	2.25
R5	1.12	1.12	1.00	1.25
R6	0.75	0.75	1.00	0.56

an axis orthogonal to the vertical axis of the robot (Fig. 2d) generates a complete turn of the robot around the same axis. Direction of robot's motion is controlled by manipulating the angle between the rotation axis of the B field and the x-axis of the workspace.

B. Actuation and Feedback Setup

As the aim of this study is to use EIT to dynamically track untethered magnetic small-scale robots, the workspace is designed as a circular arena with $30\,\mathrm{mm}$ diameter considering the average abdomen size of the mice used in preclinical studies. It is surrounded by 8 electrodes positioned equidistantly as shown in Fig. 2b. After filling the test area with $3\,\mathrm{mL}$ Phosphate Buffered Saline (PBS, P-5368 with pH 7.4, SIGMA), corresponding to a $4.24\,\mathrm{mm}$ liquid level, which is twice the width of the biggest robot in Table I, the magnetic small-scale robot is placed into this solution. To apply an external magnetic field, the test area is placed in the center of the magnetic coil setup (Fig. 2a) that can generate a 3D magnetic field within a $4\times4\times4$ cm^3 workspace with a maximum strength of $15\,\mathrm{mT}$. The magnetic field is modulated in 3D space by controlling the electric currents running through the electromagnetic coils via motor driver units (SyRen25) and an Arduino microcontroller running at $1.2\,\mathrm{kHz}$. To maintain reliable and repeatable experiments, the mapping between the applied electric currents and the generated magnetic field is calibrated regularly.

The ground truth data required to evaluate the accuracy of the proposed tracking method is collected by a high-speed camera (Basler aCa2040-90uc, shown in Fig. 2a) running at 90 fps and positioned orthogonal to the xy-plane of the workspace. Collected data (Fig. 2b) is first processed to correct the distortions and misalignments in the images, and then the position of the robot's centroid is extracted as the ground truth data.

A master PC is used to run the image processing code and the Robot Operating System (ROS), which handles all the communication tasks between different elements of the experimental setup (e.g., image capture, electric current control and EIT data collection), and allows clock synchronization between all these components.

IV. EIT TRACKING SYSTEM

A. Stimulation and Measurement Scheme

As described in Section II, EIT reconstructs the internal conductivity distribution of the test domain from electrical measurements taken at its surface for a given electrical stimulation. The stimulation pattern influences the measured data, and thereby the reconstructed images. For the sake of simplifying the implementation of EIT, drive patterns involving a single current source and sink can be preferred to strategies using multiple current sources simultaneously [38]. Bipolar drive patterns consist in injecting the current through a pair of electrodes while taking potential measurements at the remaining adjacent electrode pairs. In this work, the recently developed full scan scheme [44] is used (Fig. 2e). This scheme uses successively all possible stimulation electrode pairs to maximize the number of measurements. It has been shown to provide improved EIT images compared to the conventional adjacent and opposite strategies that rotate the current carrying electrodes through all successive adjacent and opposite electrode pairs respectively [45].

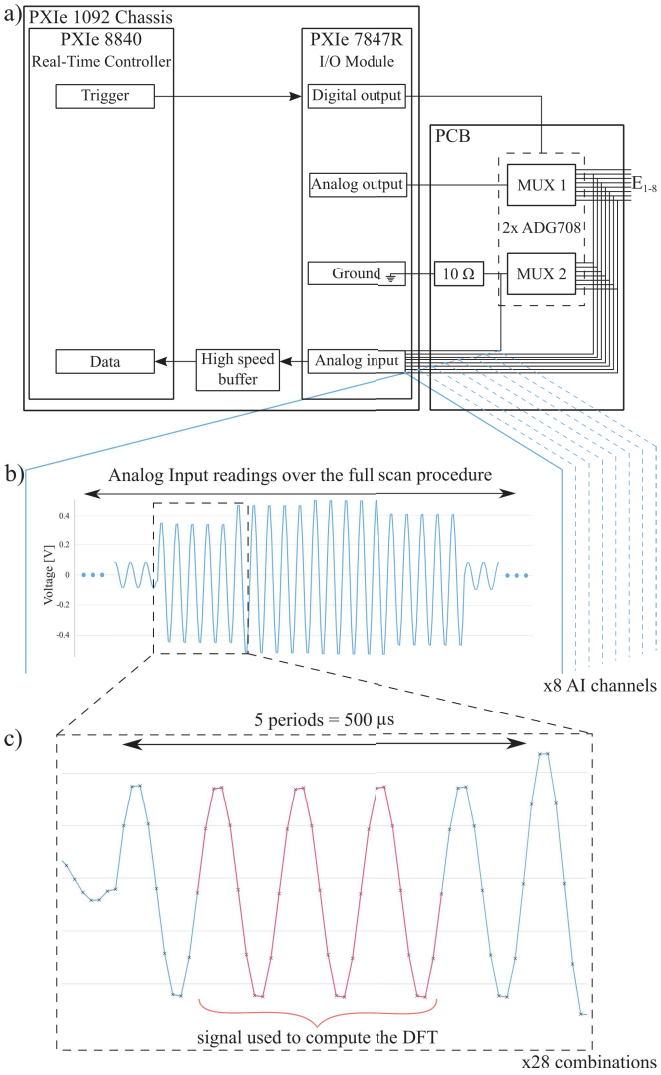

Fig. 3. a) Instrumentation used in the proposed EIT system. A real-time operating system (RTOS) controls the FPGA-based I/O module. This module both generates the stimulation sequence and measures the electrical potential of the electrodes. A $10\,\Omega$ sense resistor is used to deduce the stimulating current and normalize the measurements. All the data are sent to the host system through a high-speed buffer. b) Typical analog input readings recorded in the experiment. The combination of driving electrodes is changed every $500\,\mu\mathrm{s}$, which corresponds to 5 periods of the signal. The amplitude of the measured potentials changes accordingly. c) The sampling rate is $100\,\mathrm{kHz}$, which provides 10 data points per period. On the whole, 50 data are taken at each electrode for each combination of driving electrode-pairs. To avoid any influence of possible transient effects, the DFT is calculated over the 3 central periods only.

B. EIT Instrumentation

As sketched in Fig. 2(b, e), the workspace is surrounded by 8 evenly distributed electrodes, determined by the number of analog input channels available on the data acquisition system. The electrodes are $0.8\,\mathrm{mm}$ diameter rods made out

of platinum and connected by shielded wires to a custom-designed electronic platform (Fig. 3a) integrating two 8-to-1 multiplexers (ADG708, Analog Devices, USA). This multiplexing circuit allows to select different combinations of current carrying electrode-pairs (source and sink) to execute the entire stimulation and measurement strategy. As shown in Fig. 3a, the multiplexers are controlled by means of the digital output channels of an I/O module (PXIe-7847R, National Instruments, USA) integrating an FPGA system. The analog output and input channels of the device are respectively dedicated to the generation of the electrical stimulations and the simultaneous acquisition of the resulting electrical potentials. As previously demonstrated in [44], the stimulation signal can be an AC voltage, while the current is measured by means of a sense resistor. In the proposed system, this stimulation signal has an amplitude of $1\,\mathrm{V}$ and a frequency of $10\,\mathrm{kHz}$. The FPGA is controlled by a real-time module (PXIe-8840 Quad-Core, National Instruments, USA) and sends the recorded data to this real-time target through a Direct Memory Access (DMA) buffer. Both the I/O module and the real-time target are placed in a PXIe-1078 chassis (National Instruments, USA).

C. Signal Acquisition Procedure

While the electrical stimulation is continuously generated by the analog output of the I/O module, the digital outputs were controlled by the built-in blocks in a LabView environment to switch from a stimulation/measurement pattern to the other every $500\,\mu\mathrm{s}$. This corresponds to 5 periods of the excitation signal for each of the 28 different stimulation combinations provided by the full-scan strategy in an 8-electrode EIT system. In parallel, the electrical potential measurements are performed via the analog input channels at a sampling rate of $100\,\mathrm{kHz}$ (Fig. 3b, c).

D. Data Processing

The data are subsequently processed using the built-in libraries in the open-source software EIDORS [39]. For each stimulation combination, the Discrete Fourier Transform (DFT) of the recorded signal is determined over the 3 central periods of the recording (Fig. 3c). The first and last periods are ignored to avoid any influence of possible transient effects due to the switching from a stimulation electrode to another. The filtering of the signal is performed by taking only the element of the DFT that provides the amplitude corresponding to the excitation frequency [44]. As the amplitude of the adjacent voltages involving a current carrying electrode can be biased by the electrode polarization, these data are discarded in EIDORS. In addition, as the first analog input channel of the I/O module is used to monitor the voltage across the sense resistor and deduce the flowing current, the adjacent voltages involving $E1$ are not measured. Therefore, in each stimulation combination, 2, 3, 4 or 5 relevant output adjacent voltages can be obtained. These voltages are normalized by the amplitude of the injected current. Going over the 28 stimulation combinations, a total of $90\,(= 2 \times 5 + 8 \times 4 + 12 \times 3 + 6 \times 2)$ normalized voltages are obtained and taken as input of the EIT image reconstruction process.

As this work uses difference EIT to reconstruct conductivity changes rather than the absolute conductivity map, two datasets are needed for image reconstruction. One set is taken before the robot is inserted into the workspace, which will be referred as ”homogeneous dataset”. To reduce the influence of measurement noise in this reference dataset, it is averaged over 356 vectors of data points taken from the homogeneous medium. The other set is taken from the inhomogeneous system containing the small-scale robot, which will be referred as ”inhomogeneous dataset”.

The homogeneous and inhomogeneous datasets are taken as input of the reconstruction algorithm developed in [41] and implemented in the open-source package EIDORS [39]. This solver involves different image reconstruction parameters, which are indicated and studied in the next section. In the images generated by the reconstruction code, the workspace is discretized into multiple elements. An estimated conductivity change σ_{el} is assigned to each element and the image is generated by converting the conductivity values to a colormap.

Since the robot is known to be more resistive than the PBS solution, it is expected to correspond to a region with a highly negative conductivity change. To improve its distinguishability in the image, a threshold is imposed to the conductivity change values of the elements appearing in the reconstructed image. In other words, only significant negative conductivity changes are shown in the image, while the estimated conductivity changes σ_{el} that are positive or above the threshold are set to 0 (no color). The threshold δ_σ is defined as

$$\delta_\sigma = \overline{\sigma_{el}} - Sd_\sigma, \tag{5}$$

where $\overline{\sigma_{el}}$ is the average of the estimated conductivity value over all the elements composing the workspace and Sd_σ is the standard deviation. The thresholded image is then binarized to mark the significant elements. The center of mass of the robot is detected on the binarized image by simple shape detection after basic image processing (dilation and erosion). Remaining small isolated regions (significant negative conductivity changes) are ignored by just selecting the biggest blob in the image.

Next section describes the experiments performed to evaluate the potential of this EIT-based system for the 2D localization of a small-scale robot and presents the results of this first proof-of-concept.

V. Results

A. Effect of external magnetic field on the EIT-based localization system

As a preliminary study, the compatibility of the proposed EIT-based localization approach with the magnetic actuation system has been investigated. To identify the influence of the external magnetic field on the voltage readings, the tests have been performed using the non-magnetized set of robots (i.e., the first set of robots) whose sizes are given in Table I. Accordingly, the influence of the magnetic field on the reconstructed EIT image is analyzed while avoiding any robot motion due to magnetic actuation.

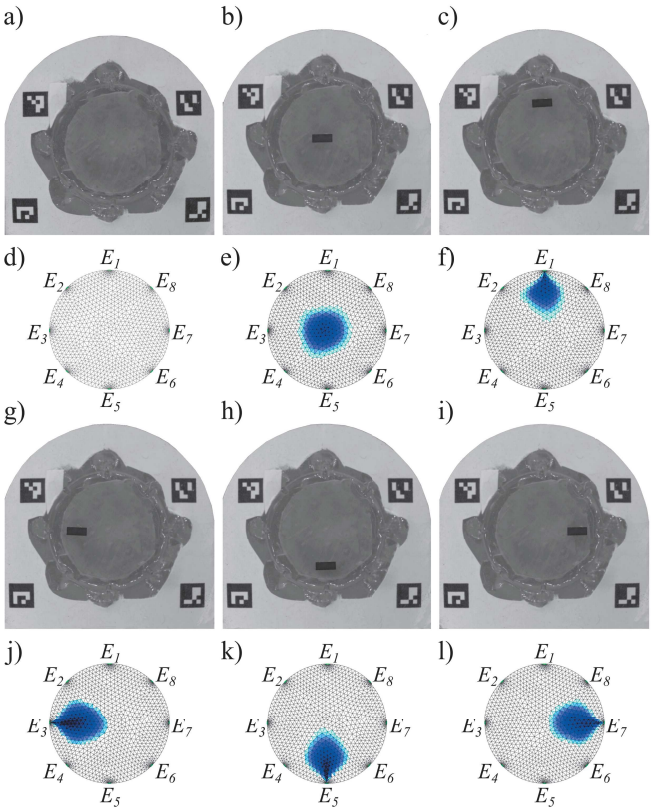

Fig. 4. Actual images (first and third rows) and the reconstruction results generated by the collected EIT data (second and fourth rows) for the static tests done with the non-magnetized robot $R1$ in Table I and $|B| = 0\,\mathrm{mT}$. For all robots with and without external magnetic field, camera and EIT images are presented in the Supplementary Material.

For this purpose four different test cases were studied: (1) $|B| = 0\,\mathrm{mT}$, without robot; (2) $|B| > 0\,\mathrm{mT}$, without robot; (3) $|B| = 0\,\mathrm{mT}$, with a robot; and (4) $|B| > 0\,\mathrm{mT}$, with a robot. In these experiments, the external magnetic field is defined as a rotating field with five different amplitude and frequency sets from $3\,\mathrm{mT}$ to $9\,\mathrm{mT}$ and from $1\,\mathrm{Hz}$ to $10\,\mathrm{Hz}$. Moreover, throughout the experiments including a robot, the robot is placed into five different positions inside the test area (Fig. 4 a-c and g-i) and each experiment is repeated five times. All EIT images are reconstructed using the solver in [41]. The resolution parameters used are $p = 0.5$, $\gamma_c = 0.9$, $\lambda = 0.05$, and $d = 5$, whose influence is explained and studied in the next subsection.

Two metrics have been used to explore the impact of the magnetic field on the EIT-based localization system. Firstly, in the experiments with the robot, the position estimations obtained from the EIT images are compared to the ground truth data obtained from the camera (Fig. 4). The position detection accuracy of the EIT system is reported in Table II with median and interquartile range (IQR) for each robot with B-Field ($B = 3\,\mathrm{mT}$, $f = 1\,\mathrm{Hz}$) and no B-Field. The camera and EIT images for each robots, and the position detection accuracy for the remaining B-Field cases are presented in the Supplementary Material. Results for both test cases show that the average localization error is the lowest for $R2$, and it increases as the size of the robot gets smaller except for $R1$ and $R6$. Moreover, due to their small size, the localization of $R5$ and $R6$ results in high error values considering the size of the workspace.

TABLE II
POSITION DETECTION ACCURACY OF THE EIT SYSTEM FOR EACH NON-MAGNETIZED ROBOT IN TABLE I THROUGHOUT THE STATIC TESTS SHOWN IN FIG. 4.

	No B-Field		B-Field (3mT 1Hz)	
Robot	Median (mm)	IQR (mm)	Median (mm)	IQR (mm)
R1	0.61	0.08	0.55	0.26
R2	0.38	0.21	0.45	0.40
R3	0.56	0.33	0.54	0.51
R4	0.70	0.61	0.58	0.74
R5	8.66	0.42	6.63	8.40
R6	3.80	13.03	7.00	4.96

TABLE III
AVERAGE CONDUCTIVITY AND CONDUCTIVITY THRESHOLD VALUES FOR THE FOUR DIFFERENT TEST CASES USED TO IDENTIFY THE INFLUENCE OF MAGNETIC FIELD ON THE EIT SYSTEM.

B-Field	Robot	Avg. Conductivity ($\overline{\sigma_{el}} \pm Sd_\sigma$)	Conductivity Threshold δ_σ	Rel. Cond. Threshold
×	×	6.17±6.93	-0.76	Ref.
3mT 1Hz	×	1.67±3.23	-1.56	106.28%
3mT 5Hz	×	-0.59±0.75	-1.33	76.36%
3mT 10Hz	×	-0.93±0.99	-1.92	153.13%
6mT 1Hz	×	-1.22±1.21	-2.43	221.07%
9mT 1Hz	×	-1.42±1.37	-2.79	268.76%
×	✓	-0.89±3.89	-4.78	531.26%
3mT 1Hz	✓	-0.10±5.53	-5.63	643.58%
3mT 5Hz	✓	-0.75±3.86	-4.61	508.94%
3mT 10Hz	✓	-0.63±4.40	-5.03	564.15%
6mT 1Hz	✓	-0.61±4.37	-4.98	557.93%
9mT 1Hz	✓	-0.61±4.39	-5.00	560.25%

Secondly, the estimated average conductivity variation in the workspace and the conductivity threshold values (δ_σ) are computed for all test cases. Table III reports the obtained values. The comparison of δ_σ values for each test case with the Case-1 given in the last column shows that application of the external magnetic field without a robot in the test area causes a maximum increase in the conductivity threshold value by 268.76%, whereas the existence of the robot without external magnetic field causes 531.26% increase. Therefore, the impact of the magnetic field on the reconstructed EIT images is shown to be smaller than the impact of the robot itself. Furthermore, the existence of the robot minimizes any visible effect of the external magnetic field on δ_σ.

To summarize, the results in Table II and Table III show that the EIT-based localization system is barely affected by the magnetic field, whose influence on the reconstructed EIT images is minor compared to the presence of the small-scale robot itself. Given the current results, the decoupling could be explained by the 4 order of magnitude difference between the frequency of the actuation signals and the frequency of the electrical signals used for localization ($1\,\mathrm{Hz}$ and $10\,\mathrm{kHz}$ respectively).

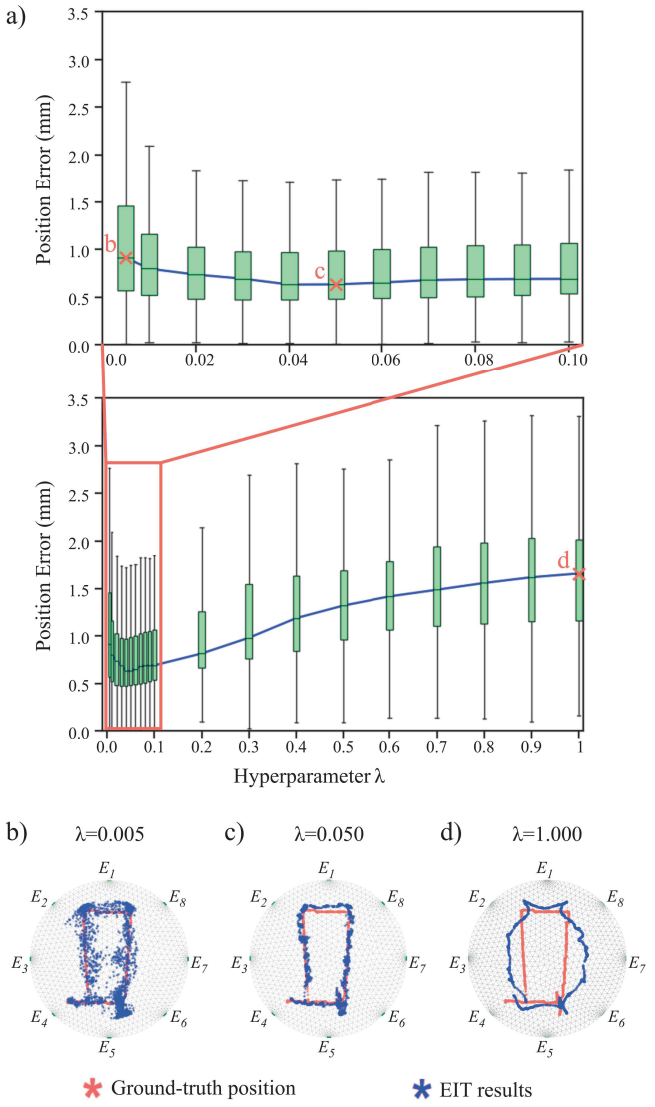

Fig. 5. Influence of the hyperparameter on the accuracy of the EIT-based tracking system. (a) Evolution of the position error over the whole trajectory as a function of the reconstruction hyperparameter λ. The whiskers represent the 2nd and 98th percentiles, while the boxes indicate the IQR and contain the median position error (blue line). The points noted b, c and d refer to the subfigures below (b, c, d) showing the position data obtained from the camera (red) and the position estimated from the electrical signals (blue). In (b), a small hyperparameter generates noise in the reconstructed trajectory. (c) Increasing the hyperparameter improves the tracking accuracy until a local optimum. (d) A smoother reconstructed trajectory is obtained using a larger hyperparameter, however at the cost of spatial resolution.

B. Dynamic Object Detection

Since the magnetic actuation and the electrical localization have been shown to be compatible within the presented experimental system, the next study uses magnetized robots (Table I) and compares the EIT-based tracking to the ground truth data obtained from the images of the camera.

1) Reconstruction parameters: As mentioned in section II, the spatio-temporal solver developed in [41] is used in this work to get EIT images of the robot moving within the workspace. Several reconstruction parameters defined therein have to be set such as the NOSER exponent p, the inter-frame

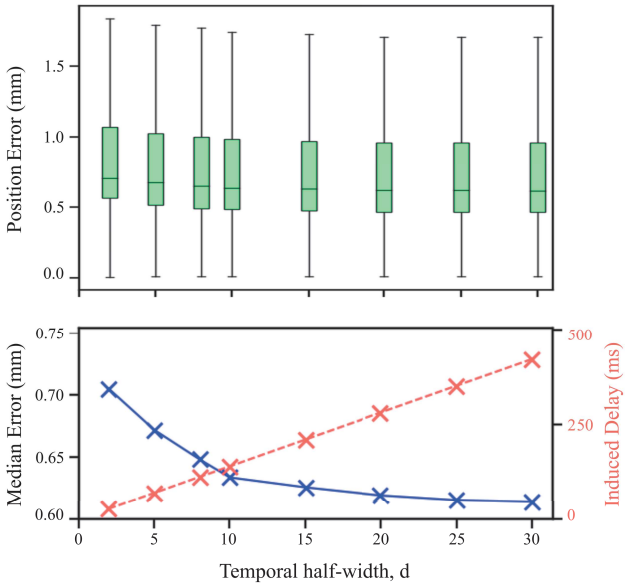

Fig. 6. Influence of the reconstruction temporal width on the accuracy of the EIT-based tracking system. While the position error (top plot) decreases with the extension of the temporal window, the delay induced in the localization increases (bottom plot).

correlation γ_c, the hyperparameter λ, and the half-width d of the temporal window. In EIT, solving the inverse problem involves a trade-off between the exact solution based on the measurements and a prior information. The exponent p is related to the spatial part of the regularization term. It tends to push the noise toward the center ($p = 1$) or the edges ($p = 0$) of the arena [41]. The parameter γ_c is involved in the temporal part of the regularization term. It reflects the correlation between successive frames. The number of frames considered in a reconstruction is determined by d. The hyperparameter λ determines the trade-off between the measurements and the known spatio-temporal information. A high value of λ increases the weight of the spatio-temporal prior information with respect to the electrical measurements, whereas a low value of λ provides an estimated conductivity closer to the exact solution based on the measurements, however at the cost of a higher sensibility to measurement noise.

The first parameter was set using a standard value from the literature [41] $p = 0.5$. $\gamma_c = 0.9$ is chosen because the data acquisition is known to be fast ($14\,\mathrm{ms}$) with respect to the dynamic of the robot. A parametric study is performed to set λ and d and highlight their impact on the accuracy of the EIT tracking. These parameters are successively varied, while reconstructing multiple times a rectangular-shaped trajectory of the robot $R2$. The impact of the hyperparameter λ on the tracking accuracy is shown in Figure 5a, while $d = 10$. A small hyperparameter degrades the tracking accuracy by generating noisy reconstructed images. On the opposite, a smooth reconstructed trajectory is obtained using a large hyperparameter, however at the cost of the spatial resolution. These results are illustrated by the trajectories obtained in the two extreme cases considered $\lambda = 0.005$ (Fig. 5b) and

$\lambda = 1$ (Fig. 5d), while the local optimum in terms of position accuracy is obtained with $\lambda = 0.05$ (Fig. 5a, c).

With $\lambda = 0.05$, the influence of the temporal window d can also be studied by a parametric sweep. Although a large temporal window provides a more accurate tracking, it induces a higher temporal delay of the obtained position information (Fig. 6). This effect is due to the fact that the reconstruction of the frame f_t uses the concatenated sequence of measurements $[y_{t-d}, ..., y_t, ..., y_{t+d}]$ [41]. In this respect, considering the $14\,\mathrm{ms}$ per frame required by the data acquisition procedure, the delay $[\mathrm{ms}]$ induced by this approach is $14 \times d$.

By choosing $d = 5$ the induced delay remains below the $100\,\mathrm{ms}$ which are induced by a position feedback system operating at $10\,\mathrm{Hz}$. This frequency is higher than the frequency reached in some recent microrobotic studies using Magnetic Resonance Imaging (MRI) as localization modality [12].

2) Tracking of different sized robots: To evaluate the capability of the proposed system to track different untethered magnetic robots, each robot (Table I) is actuated to generate 5 different trajectories. These trajectories are monitored by both the camera and the EIT tracking system. The EIT reconstruction hyperparameter $\lambda = 0.05$, which is the local optimum found in the above parametric study, while $d = 5$. Other EIT reconstruction parameters are kept same as presented above. In the Supplementary Video, one trajectory per robot is shown together with the corresponding live EIT reconstruction.

For each experiment, the median EIT-tracking error and the number of recorded positions composing the trajectory are reported in Table IV. These results show that $R4$ is the smallest robot that can be detected with a reasonable accuracy. Until $R4$, the median tracking error is lower than the length of the robot, whereas it increases significantly when the size of the robot further decreases. The results of the localization of $R5$ and $R6$ are consistent with the results of the static experiments in Section V-A (high error values). It is likely that their small size makes them undetectable by our EIT system.

Although it is bigger, $R1$ generates a higher tracking error than the one obtained for $R2$ and $R3$. This can be due to the bigger wavelets that are created by the motion of the robot at the surface of the liquid. These wavelets can change the local propagation of the electrical signal within the PBS, thus degrading the measurements and the reconstructed images. Besides, the setting of the hyperparameter has been done in the light of a parametric study performed using a trajectory of $R2$. The parameter found to be optimal may have been different if the study was done using another robot.

3) Tracking of the magnetic robot $R2$ in non-homogeneous environments: To evaluate the tracking performance of the EIT system for non-homogeneous cases, $R2$ is tested for three different scenarios (Figure 7). In each of them, two trajectories are performed and monitored by both the camera and the EIT system to quantify the tracking performance as before. The EIT reconstruction result and ground truth data of one trajectory for each test case are presented in the Supplementary Video. The EIT tracking error reported in Table V shows that the proposed tracking method can localize the robot when stationary objects are in the environment (Figure 7a, b) with a similar performance as in the homogeneous test cases. Moreover, promising results are obtained in the third test scenario (Figure 7c), where the chicken flesh covers the electrodes. Although it is necessary to tune the EIT reconstruction parameters to achieve better localization performance as in the previous test cases, these results open the door to the application of the proposed method for medical applications.

TABLE IV
POSITION DETECTION ACCURACY OF THE EIT SYSTEM GIVEN BY THE MEDIAN AND IQR FOR EACH MAGNETIZED ROBOT IN TABLE I THROUGHOUT THE DYNAMIC TESTS.

Robot	Path Number	Path Error (mm)		Robot Error (mm)		# Recorded Positions
		Median	IQR	Median	IQR	
R1	P1	0.93	0.58	0.99	0.84	3887
	P2	1.21	0.74			2974
	P3	0.66	1.37			3169
	P4	1.03	0.76			3361
	P5	0.93	0.79			2224
R2	P1	0.68	0.67	0.75	0.67	2234
	P2	0.65	0.65			2058
	P3	0.68	0.50			2236
	P4	0.86	0.77			2237
	P5	0.93	0.62			2536
R3	P1	0.82	0.81	0.87	0.79	1938
	P2	0.86	0.92			1963
	P3	0.89	0.73			2135
	P4	0.94	0.87			2279
	P5	0.82	0.64			1932
R4	P1	1.01	1.05	1.11	1.14	2260
	P2	1.44	1.38			1940
	P3	1.26	1.03			2014
	P4	0.74	0.62			1565
	P5	0.92	0.81			1644
R5	P1	6.49	2.15	6.87	2.16	2118
	P2	6.57	2.24			2194
	P3	6.79	2.31			1892
	P4	6.92	1.73			2126
	P5	7.91	2.24			2213
R6	P1	14.75	9.20	7.36	9.62	2821
	P2	8.10	7.30			2553
	P3	4.07	3.84			2003
	P4	4.92	5.13			2061
	P5	8.04	13.71			2230

VI. DISCUSSION AND OUTLOOK

This paper introduces a method based on EIT to dynamically track small-scale robots. The proposed approach provides the electrical conductivity distribution within the robot workspace from a set of electrical stimulations and voltage measurements gathered from 8 electrodes placed at its boundary. The position of the robot can be deduced from the reconstructed EIT image with the difference in electrical

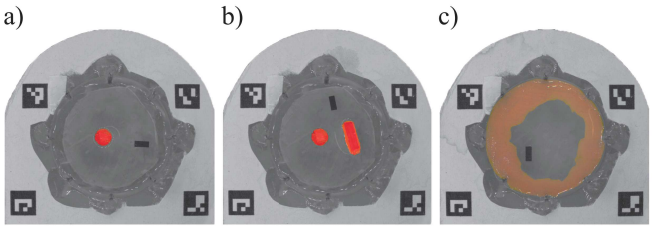

Fig. 7. Dynamic test cases with $R2$ used to evaluate the tracking accuracy of the EIT system in non-homogeneous environments. (a) Single circular stationary object in the test area, (b) multiple stationary objects with different shapes in the test area, and (c) electrodes covered by the chicken flesh.

TABLE V
POSITION DETECTION ACCURACY OF THE EIT SYSTEM GIVEN BY THE MEDIAN AND IQR FOR R2 IN TABLE I THROUGHOUT THE DYNAMIC TESTS IN NON-HOMOGENEOUS ENVIRONMENTS.

Test Case	Path Error (mm)		Robot Error (mm)		# Recorded Positions
	Median	IQR	Median	IQR	
Circular Object-1	0.76	0.68	0.92	0.78	2573
Circular Object-2	1.09	0.86			3328
Multiple Object-1	0.89	0.58	0.82	0.61	2206
Multiple Object-2	0.77	0.61			2990
Tissue-1	1.27	1.43	1.24	1.26	3304
Tissue-2	1.20	1.02			2872

properties between the robot and the background medium. Moreover, the tracking system developed in this work has been shown not to interfere with the magnetic actuation applied to the robot by testing the system with different magnetic field strengths and actuation frequencies. Multiple robots in changing sizes were fabricated and tested, while the performance of the EIT-based tracking was verified using a camera throughout the experiments. It turned out that the smallest robot that can be tracked in the cylindrical arena (30 mm in diameter) with a median position error lower than its length is 1.5 $\times$ 1.5 $\times$ 1 mm^3.

Multiple factors influence the results obtained by the proposed system in terms of tracking accuracy and smallest detectable size. As highlighted in this work, the reconstruction parameters can have a significant impact. In particular, the hyperparameter has been determined based on multiple reconstructions of a trajectory of robot $R2$ with a varying hyperparameter. As the optimal hyperparameter can be different for the other robots, a systematic parametric optimization can help improving the tracking accuracy. Beyond the heuristic method used herein, existing advanced methods can be implemented for tuning the hyperparameter such as the popular L-curve method [46], and Bayesian Optimization [43]. Similarly, rather than setting p and γ_c from standard values in the literature, these parameters could be determined from a parametric optimization.

The spatial resolution of the EIT images is also known to be strongly dependent on the number of measurements which is related to the number of electrodes [38]. Even though many EIT systems in the literature involve at least 16 electrodes [38], [44], we decided to use 8 electrodes for the sake of keeping the circuitry and the software as simple as possible. As our data acquisition system has 8 analog input channels, providing more electrodes would require to redesign the proposed EIT system. This new version would involve either using additional multiplexers, or replacing the data acquisition card by one offering more input channels, which would be more expensive. In either case, this modification would be beneficial for the spatial resolution, at the expense of the robot localization speed since the full scan scheme would involve more successive configurations. For example, using 16 electrodes leads to 120 successive configurations inducing an increase by a factor greater than 4 of the acquisition time compared to the 28 configurations obtained with 8 electrodes.

Another factor that influences the resolution and the capacity to detect a robot is the contrast in electrical properties between the robot and the background medium. The current system uses PBS whose conductivity is $1.6\,\mathrm{S\,m^{-1}}$. Although, this value is in the same order of magnitude as the conductivity of blood [47] and other physiological fluids [48], it would be interesting to evaluate the performance of our localization method in application-relevant medium in the future.

Beside its conductivity property, the liquid level also has a critical effect on the tracking performance. Throughout the preliminary tests, we observed that out of PBS motion of the robot would lead to lower tracking accuracy, as any part of the robot moving outside the liquid does not affect the impedance readings. Because of this, and also to keep the experiments as similar to the desired biomedical robotic applications as possible, we determined the amount of PBS used in the experiments twice the width of the biggest robot in Table I.

Although optical imaging remains the standard for in vitro experiments thanks to its ease of use and high resolution, the tracking accuracy obtained in this first study using EIT as a localization method in microrobotics (e.g., $0.75\,\mathrm{mm}$ and $1.24\,\mathrm{mm}$ median position errors for robot $R2$ in homogeneous test area and test area covered by chicken flesh, respectively) makes us believe that this technique could be significant and useful for the position feedback control of untethered devices for biomedical applications in the future. Moreover, it is a non-ionizing imaging method (unlike X-rays), it is portable and non-interfering with magnetic actuation (unlike MRI).

We will focus on using it together with the magnetic actuation to perform some closed-loop control inside completely enclosed spaces. As the feedback control performance depends partly on the tracking accuracy, we consider combining the EIT data to the knowledge of the expected displacement induced by the actuation (state model) by using a subsequent Kalman filter. With a data acquisition time of $14\,\mathrm{ms}$, our EIT system has the potential to provide a position feedback at a frequency of $71\,\mathrm{Hz}$. The frequency of the control loop will depend on coding aspects and the computing capacities available.

In the future, the application of this method to detect a small-scale robot in biomedical robotics raises new challenges such as the scale-up from a centimeter scale workspace to the human body, and the optimization of the number and the arrangement of the electrodes due to the complex anatomy.

ACKNOWLEDGMENT

The authors would like to thank Alp C. Karacakol for the help in designing and fabricating the softrobots. H.D. would like to gratefully thank Dr. Antoine Dupré for the instructive discussions. S.O.D. would like to thank the Ministry of National Education of the Republic of Turkey for the Doctoral Scholarship.

This work was funded in part by the Ministry of National Education of the Republic of Turkey, the Alexander von Humboldt Foundation, the Max Planck Society, and the European Research Council (ERC) Advanced Grant "SoMMoR" Project (grant number 834531). It has also been supported by the EIPHI Graduate School (contract "ANR-17-EURE-0002"), the French Agence Nationale de la Recherche and the Swiss National Science Foundation through the CoDiCell project (contract "ANR-17-CE33-0009" and "No. 00021E_175592/1", respectively), the Robotex contract "ANR-10-EQPX-44-01", and the Collegium SMYLE (SMart SYstems for a better LifE).

REFERENCES

[1] F. Ongaro, C. Yoon, F. van den Brink, M. Abayazid, S. H. Oh, D. H. Gracias, and S. Misra, "Control of untethered soft grippers for pick-and-place tasks," in *2016 6th IEEE International Conference on Biomedical Robotics and Biomechatronics (BioRob)*, Jun. 2016, pp. 299–304.

[2] B. V. Johnson, S. Chowdhury, and D. J. Cappelleri, "Local Magnetic Field Design and Characterization for Independent Closed-Loop Control of Multiple Mobile Microrobots," *IEEE/ASME Transactions on Mechatronics*, vol. 25, no. 2, pp. 526–534, Apr. 2020.

[3] J. Choi, J. Hwang, J.-y. Kim, and H. Choi, "Recent Progress in Magnetically Actuated Microrobots for Targeted Delivery of Therapeutic Agents," *Advanced Healthcare Materials*, no. 2001596, p. 24, Dec. 2020.

[4] P. Shokrollahi, Y. P. Lai, S. Rash-Ahmadi, V. Stewart, M. Mohammadigheisar, L.-A. Huber, N. Matsuura, A. E. H. Zavodni, J. Parkinson, and E. Diller, "Blindly Controlled Magnetically Actuated Capsule for Noninvasive Sampling of the Gastrointestinal Microbiome," *IEEE/ASME Transactions on Mechatronics*, pp. 1–1, 2020.

[5] S. Palagi, A. G. Mark, S. Y. Reigh, K. Melde, T. Qiu, H. Zeng, C. Parmeggiani, D. Martella, A. Sanchez-Castillo, N. Kapernaum, F. Giesselmann, D. S. Wiersma, E. Lauga, and P. Fischer, "Structured light enables biomimetic swimming and versatile locomotion of photoresponsive soft microrobots," *Nature Materials*, vol. 15, no. 6, pp. 647–653, Jun. 2016.

[6] A. Aghakhani, O. Yasa, P. Wrede, and M. Sitti, "Acoustically powered surface-slipping mobile microrobots," *Proceedings of the National Academy of Sciences*, vol. 117, no. 7, pp. 3469–3477, Feb. 2020.

[7] Y. Alapan, O. Yasa, B. Yigit, I. C. Yasa, P. Erkoc, and M. Sitti, "Microrobotics and Microorganisms: Biohybrid Autonomous Cellular Robots," *Annual Review of Control, Robotics, and Autonomous Systems*, vol. 2, no. 1, pp. 205–230, May 2019.

[8] M. Sitti and D. S. Wiersma, "Pros and Cons: Magnetic versus Optical Microrobots," *Advanced Materials*, vol. 32, no. 20, p. 1906766, 2020.

[9] H. Ceylan, I. C. Yasa, U. Kilic, W. Hu, and M. Sitti, "Translational prospects of untethered medical microrobots," *Progress in Biomedical Engineering*, vol. 1, no. 1, p. 012002, Jul. 2019.

[10] B. Wang, Y. Zhang, and L. Zhang, "Recent progress on micro- and nano-robots: towards in vivo tracking and localization," *Quantitative Imaging in Medicine and Surgery*, vol. 8, no. 5, pp. 461–479–479, Jun. 2018.

[11] S. Pané, J. Puigmartí-Luis, C. Bergeles, X.-Z. Chen, E. Pellicer, J. Sort, V. Počepcová, A. Ferreira, and B. J. Nelson, "Imaging Technologies for Biomedical Micro- and Nanoswimmers," *Advanced Materials Technologies*, vol. 4, no. 4, p. 1800575, 2019.

[12] A. Aziz, S. Pane, V. Iacovacci, N. Koukourakis, J. Czarske, A. Menciassi, M. Medina-Sánchez, and O. G. Schmidt, "Medical Imaging of Microrobots: Toward In Vivo Applications," *ACS Nano*, vol. 14, no. 9, pp. 10 865–10 893, Sep. 2020.

[13] D. Son, S. Yim, and M. Sitti, "A 5-D Localization Method for a Magnetically Manipulated Untethered Robot Using a 2-D Array of Hall-Effect Sensors," *IEEE/ASME Transactions on Mechatronics*, vol. 21, no. 2, pp. 708–716, Apr. 2016.

[14] I. S. M. Khalil, A. Adel, D. Mahdy, M. M. Micheal, M. Mansour, N. Hamdi, and S. Misra, "Magnetic localization and control of helical robots for clearing superficial blood clots," *APL Bioengineering*, vol. 3, no. 2, p. 026104, May 2019.

[15] O. Erin, M. Boyvat, M. E. Tiryaki, M. Phelan, and M. Sitti, "Magnetic Resonance Imaging System–Driven Medical Robotics," *Advanced Intelligent Systems*, vol. 2, no. 2, p. 1900110, 2020.

[16] S. Pane, V. Iacovacci, E. Sinibaldi, and A. Menciassi, "Real-time imaging and tracking of microrobots in tissues using ultrasound phase analysis," *Applied Physics Letters*, vol. 118, no. 1, p. 014102, Jan. 2021.

[17] C. Heunis, K. Behrendt, E. Hekman, C. Moers, J.-P. De Vries, and S. Misra, "Design and Evaluation of a Magnetic Rotablation Catheter for Arterial Stenosis," *IEEE/ASME Transactions on Mechatronics*, pp. 1–1, 2021.

[18] X. Yan, Q. Zhou, M. Vincent, Y. Deng, J. Yu, J. Xu, T. Xu, T. Tang, L. Bian, Y.-X. J. Wang, K. Kostarelos, and L. Zhang, "Multifunctional biohybrid magnetite microrobots for imaging-guided therapy," *Science Robotics*, vol. 2, no. 12, p. eaaq1155, Nov. 2017.

[19] S. Jeon, S. Kim, S. Ha, S. Lee, E. Kim, S. Y. Kim, S. H. Park, J. H. Jeon, S. W. Kim, C. Moon, B. J. Nelson, J.-y. Kim, S.-W. Yu, and H. Choi, "Magnetically actuated microrobots as a platform for stem cell transplantation," *Science Robotics*, vol. 4, no. 30, pp. 1–11, May 2019.

[20] D. Vilela, U. Cossío, J. Parmar, A. M. Martínez-Villacorta, V. Gómez-Vallejo, J. Llop, and S. Sánchez, "Medical Imaging for the Tracking of Micromotors," *ACS Nano*, vol. 12, no. 2, pp. 1220–1227, Feb. 2018.

[21] V. Iacovacci, A. Blanc, H. Huang, L. Ricotti, R. Schibli, A. Menciassi, M. Behe, S. Pané, and B. J. Nelson, "High-Resolution SPECT Imaging of Stimuli-Responsive Soft Microrobots," *Small*, vol. 15, no. 34, p. 1900709, 2019.

[22] R. Reale, A. D. Ninno, L. Businaro, P. Bisegna, and F. Caselli, "High-throughput electrical position detection of single flowing particles/cells with non-spherical shape," *Lab on a Chip*, vol. 19, no. 10, pp. 1818–1827, May 2019.

[23] H. Daguerre, M. Solsona, J. Cottet, M. Gauthier, P. Renaud, and A. Bolopion, "Positional dependence of particles and cells in microfluidic electrical impedance flow cytometry: origin, challenges and opportunities," *Lab on a Chip*, vol. 20, no. 20, pp. 3665–3689, Oct. 2020.

[24] J. Snyder, Y. Silverman, Y. Bai, and M. A. MacIver, "Underwater object tracking using electrical impedance tomography," in *2012 IEEE/RSJ International Conference on Intelligent Robots and Systems*, Oct. 2012, pp. 520–525.

[25] L. A. Allaud and M. H. Martin, *Schlumberger: The History of a Technique*. New York: John Wiley & Sons, 1977.

[26] A. Masner, F. Blasina, and F. Simini, "Electrical impedance tomography for neonatal ventilation assessment: a narrative review," *Journal of Physics: Conference Series*, vol. 1272, p. 012008, Jul. 2019.

[27] M. Rapin, F. Braun, A. Adler, J. Wacker, I. Frerichs, B. Vogt, and O. Chételat, "Wearable Sensors for Frequency-Multiplexed EIT and Multilead ECG Data Acquisition," *IEEE Transactions on Biomedical Engineering*, vol. 66, no. 3, pp. 810–820, Mar. 2019.

[28] X. Shi, W. Li, F. You, X. Huo, C. Xu, Z. Ji, R. Liu, B. Liu, Y. Li, F. Fu, and X. Dong, "High-Precision Electrical Impedance Tomography Data Acquisition System for Brain Imaging," *IEEE Sensors Journal*, vol. 18, no. 14, pp. 5974–5984, Jul. 2018.

[29] M. Darnajou, A. Dupre, C. Dang, G. Ricciardi, S. Bourennane, C. Bellis, and S. Mylvaganam, "High Speed EIT With Multifrequency Excitation Using FPGA and Response Analysis Using FDM," *IEEE Sensors Journal*, vol. 20, no. 15, pp. 8698–8710, Aug. 2020.

[30] Y. Zhang, R. Xiao, and C. Harrison, "Advancing Hand Gesture Recognition with High Resolution Electrical Impedance Tomography," in *Proceedings of the 29th Annual Symposium on User Interface Software and Technology*. Tokyo Japan: ACM, Oct. 2016, pp. 843–850.

[31] Z. Xu, J. Yao, Z. Wang, Y. Liu, H. Wang, B. Chen, and H. Wu, "Development of a Portable Electrical Impedance Tomography System for Biomedical Applications," *IEEE Sensors Journal*, vol. 18, no. 19, pp. 8117–8124, Oct. 2018.

[32] E. Zheng, Y. Li, Z. Zhao, Q. Wang, and H. Qiao, "An Electrical-Impedance-Tomography-Based Interface for Human-Robot Collaboration," *IEEE/ASME Transactions on Mechatronics*, pp. 1–1, 2020.

[33] K. Park, H. Lee, K. J. Kuchenbecker, and J. Kim, "Adaptive Optimal Measurement Algorithm for ERT-based Large-area Tactile Sensors," *IEEE/ASME Transactions on Mechatronics*, pp. 1–1, 2021.
[34] F. Visentin, P. Fiorini, and K. Suzuki, "A Deformable Smart Skin for Continuous Sensing Based on Electrical Impedance Tomography," *Sensors*, vol. 16, no. 11, p. 1928, Nov. 2016.
[35] J. Avery, M. Runciman, A. Darzi, and G. P. Mylonas, "Shape Sensing of Variable Stiffness Soft Robots using Electrical Impedance Tomography," in *2019 International Conference on Robotics and Automation (ICRA)*, May 2019, pp. 9066–9072.
[36] A. Adler and A. Boyle, "Electrical Impedance Tomography," in *Wiley Encyclopedia of Electrical and Electronics Engineering*. American Cancer Society, 2019, pp. 1–16.
[37] M. Cheney, D. Isaacson, and J. C. Newell, "Electrical Impedance Tomography," *SIAM Review*, vol. 41, no. 1, pp. 85–101, 1999.
[38] D. Silvera-Tawil, D. Rye, M. Soleimani, and M. Velonaki, "Electrical Impedance Tomography for Artificial Sensitive Robotic Skin: A Review," *IEEE Sensors Journal*, vol. 15, no. 4, pp. 2001–2016, Apr. 2015.
[39] A. Adler and W. R. B. Lionheart, "Uses and abuses of EIDORS: an extensible software base for EIT," *Physiological Measurement*, vol. 27, no. 5, pp. S25–S42, May 2006.
[40] Z. Zong, Y. Wang, and a. Z. Wei, "A Review of Algorithms and Hardware Implementations in Electrical Impedance Tomography," *Progress In Electromagnetics Research*, vol. 169, pp. 59–71, 2020.
[41] A. Adler, T. Dai, and W. R. B. Lionheart, "Temporal image reconstruction in electrical impedance tomography," *Physiological Measurement*, vol. 28, no. 7, pp. S1–S11, Jun. 2007.
[42] W. Hu, G. Z. Lum, M. Mastrangeli, and M. Sitti, "Small-scale soft-bodied robot with multimodal locomotion," *Nature*, vol. 554, no. 7690, pp. 81–85, Feb. 2018.
[43] S. O. Demir, U. Culha, A. C. Karacakol, A. Pena-Francesch, S. Trimpe, and M. Sitti, "Task space adaptation via the learning of gait controllers of magnetic soft millirobots," *The International Journal of Robotics Research*, p. 02783649211021869, Jun. 2021.
[44] A. Dupré, G. Ricciardi, and S. Bourennane, "Novel Approach for Analysis and Design of High-Speed Electrical Impedance Tomographic System for Void Fraction Measurements in Fast Two-Phase Flows," *IEEE Sensors Journal*, vol. 17, no. 14, pp. 4472–4482, Jul. 2017.
[45] C. Dang, C. Bellis, M. Darnajou, G. Ricciardi, S. Mylvaganam, and S. Bourennane, "Practical comparisons of EIT excitation protocols with applications in high contrast imaging," *Measurement Science and Technology*, 2021.
[46] A. Cultrera and L. Callegaro, "A simple algorithm to find the L-curve corner in the regularisation of ill-posed inverse problems," *IOP SciNotes*, vol. 1, no. 2, p. 025004, Aug. 2020.
[47] F. G. Hirsch, E. C. Texter, JR., L. A. Wood, W. C. Ballard, JR., F. E. Horan, I. S. Wright, C. Frey, and D. Starr, "The electrical conductivity of blood : I. Relationship to erythrocyte concentration," *Blood*, vol. 5, no. 11, pp. 1017–1035, Nov. 1950.
[48] Y. Lu, T. Liu, A. C. Lamanda, M. L. Y. Sin, V. Gau, J. C. Liao, and P. K. Wong, "AC Electrokinetics of Physiological Fluids for Biomedical Applications," *Journal of Laboratory Automation*, vol. 20, no. 6, pp. 611–620, Dec. 2015.

Hugo Daguerre received his M.Sc. in Mechanical Engineering from the National Institute of Applied Sciences of Lyon, France, in 2018. He is currently a PhD Student in the Department of Automation, Microsystems and Mechatronics at the Femto-ST Institute (CNRS), France, and came to the Max Planck Institute for Intelligent Systems as a visiting PhD student in 2020. His research interests include microrobotics, microfluidics, and autonomous small-scale devices for biomedical applications.

Sinan Ozgun Demir received his B.Sc. and M.Sc. degrees in Mechanical Engineering from Middle East Technical University, Ankara, Turkey in 2014, and 2017. He is currently a Ph.D. student in the Physical Intelligence Department at the Max Planck Institute for Intelligent Systems and the Stuttgart Center for Simulation Science at the University of Stuttgart. His research focuses on adaptive actuation of the magnetic small-scale soft robots using machine learning methods.

Utku Culha received his B.Sc. and M.Sc. degrees in Computer Engineering from Bilkent University, Turkey and Dr.Sc. degree in Mechanical and Process Engineering from ETH-Zürich, Switzerland in 2016. He was a research scientist at the University of Cambridge during 2014-2016. He received the Alexander von Humboldt postdoctoral research fellowship and worked as a senior scientist at the Physical Intelligence Department at the Max Planck Institute for Intelligent Systems in Stuttgart, Germany between 2016 and 2021. He is the Chief of Science of the Munich School of Robotics and Machine Intelligence at the Technical University of Munich, Germany (2021). His research focuses on building physically adaptive robotic systems using functional soft materials, biological inspirations, machine learning, and self-assembly.

Francois Marionnet received his M.Sc. in Electronics and Microelectronics Engineering from the Institute of Chemistry, Physics and Electronics of Lyon (ICPI Lyon, renamed CPE Lyon then ESCPE Lyon), France, in 1995. He is currently a Research Engineer in the Department of Automation, Microsystems and Mechatronics at the Femto-ST Institute, Besancon, France. As an expert in the development of electronic systems, he is involved in various research projects in microrobotics and automation.

Michaël Gauthier, CNRS senior scientist, works in the field of micro-nanorobotics since 2000 and has proposed, modeled and experimented new robotics tools for microhandling and micro-assembly in several European and National projects. He is the president of the French-Swiss Alliance between FEMTO-ST and EPFL named SMYLE. During the last years, he was the head of the micro-nanorobotics department in FEMTO-ST (2012-16) and vice-director of FEMTO-ST institute (2016-19). He is the author of 2 books, more than 40 papers and 60 conference talks. He is also the co-founder of the spin-off 'Percipio Robotics' providing micro-assembly platforms for industrial applications.

Metin Sitti received the BSc and MSc degrees in Electrical and Electronics Engineering from Bogazici University, Turkey, and the PhD degree in Electrical Engineering from the University of Tokyo, Japan, in 1999. He was a research scientist at University of California at Berkeley during 1999–2002 and a professor of Mechanical Engineering and Robotics Institute at Carnegie Mellon University, USA during 2002–2016. Since 2014, he has been the director of the Physical Intelligence Department at the Max Planck Institute for Intelligent Systems in Stuttgart, Germany. His research interests include small-scale physical intelligence, mobile milli/microrobots, bio-inspiration, advanced functional micro/nanomaterials, and medical microrobotics.

Aude Bolopion received her Ph.D. degree in robotics in 2010 from the University of Pierre et Marie Curie, Paris, France. She is currently a CNRS researcher at the FEMTO-ST Institute, Besancon, France. She has been awarded the French CNRS bronze medal (Early Career Award) in 2019. Her research interests are focused on non-contact manipulation and untethered microrobotics.